HHS Public Access

Author manuscript

ACS Appl Mater Interfaces. Author manuscript; available in PMC 2021 September 23.

Published in final edited form as:

ACS Appl Mater Interfaces. 2020 September 23; 12(38): 42499–42510. doi:10.1021/acsami.0c10781.

Polydopamine-Mesoporous Silica Core-Shell Nanoparticles for Combined Photothermal-Immunotherapy

Anushree Seth[†,Ω], **Hamed Gholami Derami**[†,Ω], **Prashant Gupta**[†], **Zheyu Wang**[†], **Priya Rathi**, **Rohit Gupta**[†], **Thao Cao**, **Jeremiah J. Morrissey**[§], **Srikanth Singamaneni**[†,*]

[†] Department of Mechanical Engineering and Materials Science, Institute of Materials Science and Engineering, Washington University in St. Louis, Saint Louis, MO 63130, USA

[§] Department of Anesthesiology, Siteman Cancer Center, Washington University in St. Louis, St. Louis, MO, 63110, USA

[ɣ] Department of Chemistry, Washington University in St. Louis, Saint Louis, MO 63130, USA

[ħ] Department of Biomedical Engineering, Washington University in St. Louis, St. Louis, MO 63130, USA

Abstract

Cancer immunotherapy involves a cascade of events that ultimately leads to cytotoxic immune cells effectively identifying and destroying cancer cells. Responsive nanomaterials, which enable spatiotemporal orchestration of various immunological events for mounting a highly potent and long-lasting anti-tumor immune response, are an attractive platform to overcome challenges associated with existing cancer immunotherapies. Here, we report a multifunctional near infrared (NIR)-responsive core-shell nanoparticle, which enables (i) photothermal ablation of cancer cells for generating tumor associated antigen (TAA) and (ii) triggered release of an immunomodulatory drug (gardiquimod) for starting a series of immunological events. The core of these nanostructures is composed of polydopamine nanoparticle, which serves as a photothermal agent, and the shell is made of mesoporous silica, which serves as a drug carrier. We employed a phase-change material as gatekeeper to achieve concurrent release of both TAA and adjuvant, thus efficiently activating the antigen presenting cells (APCs). Photothermal-immunotherapy enabled by these nanostructures resulted in regression of primary tumor and significantly improved inhibition of secondary tumor in a mouse melanoma model. These biocompatible, biodegradable, and NIR-responsive core-shell nanostructures simultaneously deliver payload and cause photothermal

[*]Corresponding Authors singamaneni@wustl.edu.
[Ω]These authors contributed equally to this work

The authors declare no competing financial interests.

Supporting Information

Analysis of TGA data; Loading and release of LT680; Photothermal efficiency calculation; SEM image of as-prepared silica-coated PDA nanoparticles before removing the pore-template (CTAB); HRTEM image of PDA@$mSiO_2$ nanoparticles and corresponding EDS elemental mapping for N and Si; Absorbance spectra of PDA and PDA@$mSiO_2$ nanoparticles; TEM images of the PDA@$mSiO_2$ nanoparticles before and after 10 minutes laser treatment; *In vitro* maturation of BMDCs; Fluorescence images showing efficient dye loading without free dye in solution and NIR-triggered release of LT680 dye from PDA@$mSiO_2$; Nanoparticle uptake by cancer cells; Absorption and emission spectra of CFSE and LT680; Infrared images, fluorescence images and changes in local temperature of the mouse melanoma model; Relative populations and activation status of immune cells in tumor draining lymph node; Therapeutic effect of increasing NIR treatment duration to 10 minutes.

ablation of the cancer cells. Our results demonstrate potential of responsive nanomaterials in generating highly synergistic photothermal-immunotherapeutic response.

Graphical Abstract

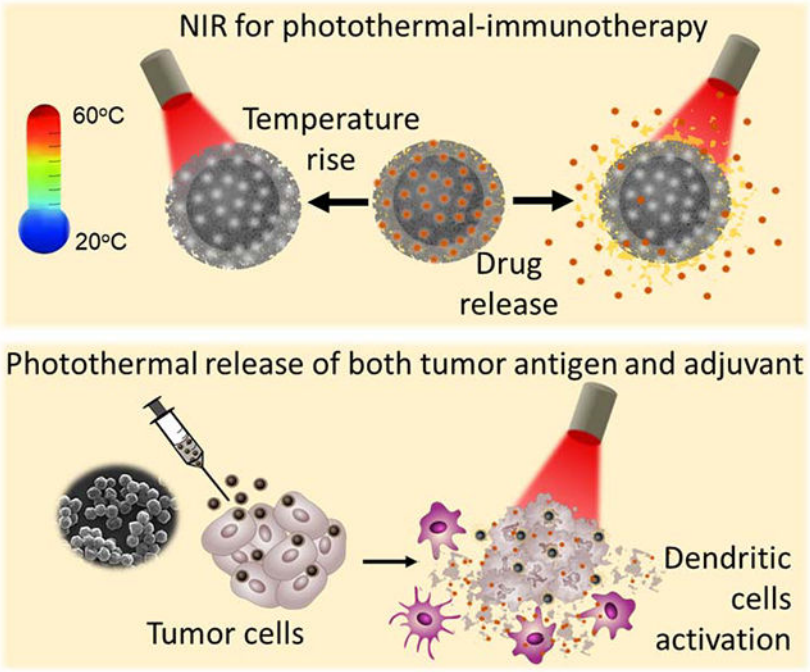

Keywords

cancer immunotherapy; mesoporous silica; NIR-responsive drug delivery; polydopamine nanoparticles; photothermal therapy

Introduction

Immunotherapy has proven to be a successful therapeutic approach for cancer with long-lasting effects. However, only a limited fraction of patients is completely cured by standalone immunotherapy. A primary cause of the low response rate is the "immunoediting" employed by cancer in an immuno-competent host to escape surveillance.[1–3] Cancer cells downregulate antigenic proteins and peptides, upregulate immune-inhibitory receptors and express/secrete immuno-suppressive factors to effectively create a pro-tumor microenvironment.[4] The primary goal of immunotherapeutic interventions is to restore the lost immunogenicity and reverse the immuno-suppressive microenvironment in the tumor.[5–6] Toll-like receptor (TLR) agonists and immunomodulatory vaccine adjuvants such as polyinosinic:polycytidylic acid (Poly(I:C)), cytosine-phosphorothioate-guanine (CpG), imiquimod, and resiquimod reprogram the tumor microenvironment (TME). These TLR agonist act either alone or in combination with other treatment modalities such as chemotherapy, photodynamic therapy (PDT), radiotherapy or photothermal therapy (PTT) for generation of potent anti-tumor immune response.[7–16]

An ideal combination immunotherapy involves a “tumor killing” modality including PTT, PDT, or chemotherapy, that should partially ablate the tumor and release tumor-associated antigens (TAAs) and damage associated molecular patterns (DAMPs). The released TAAs and DAMPs synergize with immunomodulatory drugs to create a tumor-inhibitory environment. In previous studies, the two components-i) chemo/photothermal/photodynamic agents; and ii) the immunomodulators, are co-delivered either in the form of a simple physical mixture or co-encapsulated in a drug delivery vehicle.[17–21] With these therapeutic approaches, there is no external control over the release profile or the bioavailability of the therapeutic agents once the formulation is administered inside the body. The lack of external control over the cargo release leads to differential release kinetics of antigen and adjuvant. This compromises the efficacy of the innate immune response and subsequent adaptive immune response. For eliciting cytotoxic anti-tumor immune response, the internalized antigen must undergo cross-presentation, which includes MHC I-restricted presentation to $CD8^+$ T cells.[22–23] For optimum cross-presentation by APCs, the antigen and adjuvant should preferentially be exposed simultaneously to the APCs.[24] If the APCs are exposed to adjuvant first, it leads to their activation and maturation, which in turn leads to down-regulation of phagocytosis and cross-presentation compromising the overall anti-tumor immunity.[25–26] On a contrary, if the APCs are exposed to antigen first in the absence of adjuvants, then the APCs cross-present the antigen in the absence of co-stimulatory receptors (e.g., CD40, CD80), which leads to generation of immunological tolerance and anergy.[27–29] Both of these scenarios (antigen first in the absence of adjuvant and *vice versa*) result in sub-optimal anti-tumor immune response, thus underscoring the importance of innovative delivery approaches for spatiotemporally orchestrating the availability of antigens and adjuvant for APCs.

Here, we aim to achieve simultaneous release of TAAs and adjuvant using photothermal immunotherapy. Towards this goal, we have designed and synthesized polydopamine (core) - mesoporous silica (shell) nanostructures that enable photothermal tumor ablation owing to the photothermal properties of the PDA nanostructures and simultaneous release of the adjuvant contained in the mesoporous silica shell. Recently, polydopamine has attracted increased attention as a bio-inspired, biocompatible, and biodegradable photothermal material for various biomedical applications.[30–40] Mesoporous silica, which is employed as shell, exhibits excellent biocompatibility, and complete degradation into non-toxic components making it an attractive candidate as a drug carrier.[41] We harnessed mesoporous silica shell for controlled release of gardiquimod, a toll-like receptor 7/8 (TLR 7/8) agonist, known to improve cell-based or combination immunotherapies for various cancers.[42–45] Mesoporous silica was loaded with a mixture of gardiquimod and a phase change material, 1-tetradecanol, which served as a “gate keeper” for near infrared (NIR) light-controlled release of the cargo. We engineered the core-shell nanoparticles to generate locoregional heat to ablate the tumor cells and simultaneously release the adjuvant through melting of the phase change material upon heating caused by NIR irradiation (Figure 1A). The concurrently released antigens (upon tumor ablation with NIR irradiation) and adjuvant causes effectual activation of dendritic cells, which in turn activate the $CD8^+$ T cells in the tumor draining lymph nodes. The activated cytotoxic effector T cells not only eliminate the residual primary tumor but also inhibits recurrent secondary tumors (Figure 1B). Using these

multifunctional nanoparticles, we demonstrate robust photothermal-immunotherapeutic response using NIR light as an external trigger.

Experimental Section

Preparation of PDA nanoparticles coated with mesoporous silica shell (PDA@mSiO2):

All chemicals are purchased from Millipore Sigma, St. Louis, MO, USA and used without further purification, unless or otherwise mentioned. Polydopamine nanoparticles were synthesized by using a method reported previously.[46] Briefly, 112 mL of ethanol was mixed with 252 mL of deionized (DI) water (resistivity of 18.2 MΩ·cm) in a glass container. Subsequently, 4.2 mL of aqueous solution of ammonia (28−30% NH_4OH) was added into the above water/ethanol mixture. After stirring for 30 minutes, dopamine hydrochloride (1.4 g in 28 mL water) was added to the reaction mixture. The reaction was left under gentle magnetic stirring for 24 hours. The PDA particles were collected by centrifugation (9000 rpm, 10 minutes) and washed with DI water five times and dispersed in water.

To form mesoporous silica shell on PDA particles, 0.8 ml of polydopamine solution (8 mg/ml in water) was mixed with 0.4 ml of cetyltrimethylammonium bromide (CTAB, 0.1 M) and stirred at 30 °C for 10 minutes. Then, 0.2 ml tetraethyl orthosilicate (TEOS, 17% v/v in ethanol) was added to the mixture under vigorous stirring. After 10 minutes, 5 μl of ammonium hydroxide (NH_4OH, 30% in water) was added and the mixture was left stirring at room temperature for 15 hours. The core-shell particles were washed three times with water and then three times with ethanol and dispersed in ethanol. To remove the template of CTAB, particles were dispersed in ammonium nitrate solution (NH_4NO_3, 60 ml, 10 mg/ml in ethanol) and refluxed at 45 °C for 24 hours. The mesoporous silica-coated PDA nanoparticle were washed five times with ethanol and dispersed in ethanol.

Drug Loading :

Loading of drugs into PDA@$mSiO_2$ nanoparticles using 1-tetradecanol (TD) as gatekeeper was carried out following previous reports with some modifications.[47] Typically, 1-tetradecanol (4 mg) was mixed with gardiquimod 1-(4-amino-2-ethylaminomethylimidazo-[4,5-c]quinolin-1-yl)-2-methylpropan-2-ol (50 μl, 5 mg/ml in ethanol) in a round-bottom glass tube. The glass tube was heated to 75 °C under mild stirring and left for 20 minutes. Subsequently, PDA@$mSiO_2$ nanoparticle solution (8 mg in 200 μl ethanol) was added to the mixture and temperature was increased to 90 °C. The mixture was stirred for about 1 hour until the ethanol completely evaporated. The particles were resuspended by adding hot water (1 ml, 80 °C) followed by sonication for 5 seconds. The mixture was immediately centrifuged (9000 rpm, 10 min) and supernatant discarded. Drug-loaded particles were dispersed in cold water and washed with water 10 times to remove free drug in solution. The loading amount of gardiquimod was measured by dispersing the gardiquimod-loaded nanoparticles in acetone followed by 20 minutes of sonication to extract the gardiquimod and TD into acetone. The UV-vis absorption at 329 nm was used to estimate the amount of loaded gardiquimod. The drug loading efficiency was calculated according to the following equation:

$$\text{Encapsulation efficiency} = \frac{\text{mass of drug loaded (μg)}}{\text{mass of nanoparticle (mg)}}$$

To load the Rose Bengal and LT680 dyes, similar procedure was followed. The loading amount for Rose Bengal (UV absorption at 545 nm) was found to be 11.25 μg/mg.

Nanoparticle characterization

Transmission electron microscope (TEM) images were obtained using a JEOL JEM-2100F field emission microscopy. Scanning electron microscopy (SEM) images were obtained using a JEOL JSM-7001 LVF field-emission scanning electron microscope. High resolution transmission electron microscope (HRTEM) images and energy-dispersive X-ray spectroscopy (EDX) elemental mappings were obtained using a JEOL JEM-2100F field-emission STEM. Thermogravimetric analysis (TGA) was performed in nitrogen using a TA Instruments Q5000 IR thermogravimetric analyzer at a heating rate of 5 °C minute^{-1}. Dynamic light scattering (DLS) and zeta potential measurements were performed using Malvern Zetasizer (Nano ZS). Shimadzu UV-1800 spectrophotometer was employed for light absorption measurements. The pore size distribution was estimated from nitrogen adsorption/ desorption isotherms by using Barrett-Joyner-Halenda (BJH) method and a surface area analyzer (Autosorb-1C).

NIR-induced heating and drug release profiles

Aqueous solutions of pristine PDA@mSiO_2 nanoparticles at different concentrations (0–1000 μg/ml) were prepared in a 1 ml cuvette. NIR laser (808 nm) was placed on top of the cuvette at a distance of ~10 cm to deliver 14 mW/mm^2 power density to the top of the solution. The temperature rise for different particle concentrations was monitored over 9 minutes by an IR camera (ICI 7320 USB camera). Temperature rise of water under identical irradiation conditions was recorded for comparison.

For probing the NIR-triggered release profile, rose bengal (RB) was used as a model dye. 1 ml of RB-loaded PDA@mSiO_2 nanoparticles was concentrated to 400 μl solution. 200 μl of the concentrated particles was irradiated by NIR laser (808 nm) at power density of 14 mW/mm^2. At specific times during laser treatment, 15 μl of the solution was extracted and diluted to 400 μl in water and centrifuged immediately. The optical absorbance of RB within the supernatant was measured using UV-vis spectrometer. The corresponding solution temperature for each time point was measured using an IR camera. Similar procedure was followed for NIR-triggered release of LT680 (fluorescent dye) from PDA@mSiO_2 nanoparticles. The LICOR Odyssey CLx scanner was used to measure the fluorescence intensity of the supernatant.

Cell culture, BMDC isolation and animal model

The B16-F10, a murine melanoma cell line, was purchased from American type culture collection (ATCC). Cells were maintained in Dulbecco's Modified Eagle's Medium (DMEM, Gibco) with 10% fetal bovine serum (FBS, Gibco), 100 U/ml penicillin and 100 μg/ml streptomycin. Female C57BL/6 (H-2b) mice that were 6 to 8 weeks of age were

purchased from Jackson Labs (Bar Harbor, ME, USA). The mice were maintained under pathogen-free conditions. All experiments employing mice were performed in accordance with laboratory animal protocol approved by the School of Medicine Animal Studies Committee of Washington University in St. Louis. Mouse were euthanized using CO_2 asphyxiation and cervical dislocation. The euthanized mouse was kept in 70% (v/v) ethanol for 1 min. Both the femurs and tibiae were isolated, and the muscle attachments were carefully removed using gauze pads. Both ends of the bones were cut with scissors and the marrow was centrifuged in an adapted centrifuge tube (0.6 ml tube with a hole inserted in 1.5 ml tube) at 1000 rpm for 10 seconds. The pellet was resuspended by vigorous pipetting in RPMI 1640 media. The cells were passed through a 70 μm cell strainer to prepare a single cell suspension. After one wash (1200 rpm, 5 min), red blood cells were depleted with RBC lysis buffer (Sigma-Aldrich). The bone marrow cells were collected and cultured in 100-mm Petri dishes containing 10 ml RPMI medium supplemented with 10% heat-inactivated FBS, 50 IU/ml penicillin, 50 μg/ml streptomycin, and 20 ng/ml mouse recombinant granulocyte-macrophage colony-stimulating factor (GM-CSF, R&D Systems, MN, USA).

Photothermal cytotoxicity assay

For probing the photothermal efficacy of PDA@$mSiO_2$ nanoparticles, 1×10^4 B16-F10 cells in 100 μl of media/well were seeded in a 96-well plate and kept at 37°C with 5% CO_2 for 12 hours. Cells were incubated with different concentrations of PDA@$mSiO_2$ nanoparticles for 6 hours after which they were subjected to 808 nm laser for 10 minutes at a power density of 14mW/mm^2. After 24 hours, MTS assay was performed as per manufacturer protocol.

BMDC activation and maturation

BMDCs (1×10^6) were seeded on a 6-well plate in 1 ml of media. The cells were treated with supernatants collected after centrifuging 100 μg/ml gardi-mPDA nanoparticles at 8000 rpm for 10 minutes. For gardi-mPDA-NIR, the particles were treated with 10 minutes of 808 nm laser (14mW/mm^2) right before centrifugation. The collected supernatants were added to BMDCs and incubated for 24 hours. The cells were harvested using a cell scraper and centrifuged at 1000 rpm for 5 minutes. The supernatant was used for assessment of cytokine (IL-6 and TNFα) levels using ELISA (R&D Systems, Minneapolis, USA). The cells were fixed using 10% neutral buffered formalin (NBF) for 20 minutes at room temperature and then washed with PBS. The cells were then blocked using CD16/CD32 (Mouse BD Fc Block™) and stained for APC-CD40 and PE-CD80 followed by analysis using flow cytometry (Acea Novocyte, San Diego, USA).

Uptake of nanoparticles

For studying the uptake of the nanoparticles, BMDCs were treated with 100 μg/ml of LT680-mPDA. After incubating for 1 hour, the cells were washed and fixed with 10% NBF (20 minutes) followed by washing three times with PBS. NIR laser was treated for 2 minutes to release some dye and prevent the LT680 self-quenching. The cells were then stained with DAPI using manufacturer's protocol. The images were acquired using Zeiss LSM 880 Confocal fluorescence microscope.

In vitro combined photothermal and immune-stimulation study

For probing the combined photothermal and immune-stimulation efficacy of nanoparticles, 1×10^6 B16-F10 cells per well were seeded in a 6 well plate followed by incubation with either LT680-mPDA or gardi-mPDA nanoparticles (100 μg/ml). After incubating with the nanoparticles for 1 hour, cells were harvested and washed three times with PBS (1100 rpm, 5 minutes). The cells were then stained with 1 μl of CellTrace™ CFSE (Invitrogen™, Carlsbad, USA) for 20 minutes at room temperature. The cells were then washed with complete media and divided into two groups of 2×10^6 cells in 100 μl of culture medium. The first group was subjected to 10 minutes of 808 nm laser (14 mW/mm^2) treatment, followed by dilution of cells in 1 ml of culture medium. The second group was directly diluted in 1 ml of medium and the cells from both the groups were seeded in a 6-well plate for incubation at 37ºC for 12 hours. Cells were harvested and centrifuged at 1100 rpm for 5 minutes. The LICOR Odyssey CLx scanner was used to measure the fluorescence intensity of the LT680 and fluorescence plate reader (Molecular devices, SpectraMax ID3) was used to measure the fluorescence intensity of CFSE in the supernatant. For immune-stimulation study B16-F10 cells were treated with gardi-mPDA instead of LT680-mPDA as described above. The supernatants collected from the two groups were treated on BMDCs (1×10^6) seeded in a 6-well plate. Supernatant from BMDCs was collected 24 hours post-treatment and the IL-6 secretion was measured using ELISA (R&D Systems, Minneapolis, USA).

In vivo photothermal efficacy and drug release

Photothermal treatment was performed 1 day post-injection of PDA@$mSiO_2$ nanoparticles into the tumor site. Mouse injected with gardi-mPDA was anaesthetized and subjected to 808 nm laser (power density of 14 mW/mm^2 and laser spot size of 5 mm). The body hair was removed from the tumor site to eliminate the external factors affecting the photothermal heating. The tumor injected with gardi-mPDA nanoparticles was irradiated with laser for 5 minutes. The corresponding tumor surface temperature was measured using an IR camera. Identical NIR irradiation was performed on a tumor-inoculated mouse without particle injection to collect the tumor surface temperature during treatment, as a control.

For drug release experiment, 7 days after B16-F10 tumor inoculation, mice were scanned using LICOR scanner for background fluorescence. Then 10 μl of LT680-mPDA were adminstered intratumorally, followed by fluorescence imaging one immediately and the other 10 minutes after adminstration. The mice were then subjected to 14 mW/mm^2 808 nm laser treatment for 5 minutes and then imaged. Fluorescence intensity (FI) after particle injection was considered as a reference and the fold increase was calculated for 10 minutes without NIR and with NIR.

In vivo tumor model

Six to eight weeks old C57Bl/6 mice were inoculated on the right flank with 1×10^6 B16-F10 cells (s.c) in 100 μl of HBSS. On day 6, mice bearing tumor with a diameter of 4–6 mm were selected, numbered and divided into 4 groups (n=7). The mice in different groups were administered 50 μl of PBS, gardi-mPDA, PDA@$mSiO_2$ and gardi-mPDA intra-tumorally. At 24 hours after injection, PDA@$mSiO_2$ and one gardi-mPDA group was treated with 808 nm laser (14 mW/mm^2) for 5 minutes. A 24-hours allows diffusion within the tumor and uptake

of injected nanoparticles by the cancer cells. The body weight and tumor diameters were measured every other day till day 19 after tumor implantation using a sliding caliper. Tumor volume was calculated as following: tumor volume = length × $(width)^2/2$. For survival study, the treated animals were observed for at least 42 days. For secondary tumor challenge, tumor-free mice at day 28 were re-challenged with 5×10^5 B16-F10 cells on the opposite flank. For histopathological analysis, the heart, kidney, liver, spleen and lungs were harvested 2 weeks after immunization and processed for hematoxylin−eosin staining.

In vivo flow cytometry analysis

To assess the population of immune cells in tumor draining lymph nodes, the inguinal lymph node from the tumor bearing side was isolated and digested using 0.5 mg/ml collagenase I and 0.1 mg/ml DNAase in DMEM at 37°C for 1 hour. Nylon mesh filter (70 μm) was used to prepare single cell suspension followed by washing three times with PBS. The cells were subjected to blocking using CD16/CD32 (Mouse BD Fc Block™), followed by staining with FITC-CD11c, PE-Dazzle-CD3, FITC-CD8, APC-CD40, PE-CD80 and Per CP-MHC II (eBiosciences, San Diego, USA) for 1 hour at room temperature in dark. The cells were washed three times with PBS and then analyzed using flow cytometry (Acea Novocyte, San Diego, USA). We performed pulse geometry gating to gate single cells and exclude any doublets. We plotted height vs area (FSC-H vs FSC-A) and gated single cells falling along the diagonal. For statistical analysis, a total 10,000 cells from first plot were analyzed by sub-setting gating strategy. For this analysis, the single cells were analyzed for expression levels of two surface receptors and using a quadrant gate, the cells in top-right quadrant were assigned as double positive for both receptors (as shown in Figure S7C).

Statistical analysis

For analyzing the statistical difference between two groups, unpaired two-tailed t-test with Welch's correction was used. For analyzing the statistical difference between more than two groups, one-way ANOVA with post-hoc Tukey's honest significance test was used. Statistical significance of the data was calculated at 95% ($p < 0.05$) CIs. For analyzing statistical significance in survival data log-rank (ManteleCox) test was used. All values are expressed as mean ± standard deviation from three or more independent or repeated experiments. GraphPad Prism 6 (San Diego, CA, USA) was used for all statistical analysis and Origin and GraphPad was used for creating all figures.

Results and Discussion

Synthesis and characterization of mesoporous silica-polydopamine nanoparticles (PDA@mSiO$_2$)

Spherical PDA nanoparticles are synthesized by oxidative self-polymerization of dopamine monomer in water−ethanol−ammonium mixture at room temperature.[46] By controlling the amount of ammonium hydroxide, spherical PDA particles with a diameter of 180 ± 20 nm were synthesized (Figure 2A, E). Subsequently, silica shell was formed around the PDA nanoparticles using modified Stöber method.[48] For forming nanoscale pores within the silica shell, cetyltrimethylammonium bromide (CTAB), which serves as a porogen, was added to the reaction mixture. Following the formation of the shell, CTAB was removed through ion

exchange.[49] The resulting core-shell nanostructures exhibited highly porous structure with buckled surface (Figure 2B, F). The as-prepared silica-coated PDA nanoparticles did not exhibit buckling on their surface (Figure S1). The surface buckles appeared after refluxing the core-shell particles in ammonium nitrate solution to remove the porogen (*i.e.* CTAB). The differential thermal stresses at the core-shell interface developed during reflux process (at 45°C for 24 hours) possibly result in the buckled surface morphology of the nanostructures. The particle size of PDA@$mSiO_2$ nanoparticles was found to be 340 ± 40 nm measured from TEM and SEM images using ImageJ software (Figure 2B, F). The thickness of the mesoporous silica coating was found to be ~80 nm calculated from the difference between size of PDA and PDA@$mSiO_2$ nanoparticles. Both PDA and PDA@$mSiO_2$ exhibited negative zeta-potential (~−30 mV) at physiological pH of 7.4 (Figure 2D). The pore size distribution of the PDA@$mSiO_2$ nanoparticles exhibited a sharp peak at 3.1 nm, confirming the mesoporous nature of the shell (Figure 2G). Scanning transmission electron microscopy-energy dispersive X-ray spectroscopy elemental mapping of N and Si delineated the PDA core and silica shell, as evidenced by the presence of N and Si in the core and shell, respectively (Figure S2). Thermogravimetric analysis (TGA) of the pristine PDA nanoparticles and PDA@mSiO2 nanoparticles indicated that silica shell corresponds to about 36% of the weight of the PDA@mSiO2 nanoparticles (Figure 2H).

Photothermal and controlled release properties of PDA@$mSiO_2$ nanoparticles:

Polydopamine and PDA@$mSiO_2$ nanoparticles exhibited broad light absorption over visible and NIR parts of the electromagnetic spectrum (Figure S3A). To explore the NIR-induced heating of PDA@$mSiO_2$ nanoparticles and dynamics of the temperature increase, different concentrations of PDA@$mSiO_2$ nanoparticles in water were subjected to 808 nm laser irradiation at a power density of 14 mW/mm^2. For 300 seconds of laser irradiation, the temperature increased monotonically and reached to a maximum of 57°C for PDA@$mSiO_2$ nanoparticles solution with a concentration of 1000 μg/ml (Figure 3A). As expected, the maximum temperature increased with an increase in the nanoparticle concentration (Figure 3B). Temperature rise of the core-shell nanoparticle solution under NIR irradiation ranged from 10°C to 30°C for concentrations ranging from 100–1000 μg/ml. In contrast, temperature of de-ionized water increased by only 2°C under identical NIR irradiation conditions. Following the NIR irradiation for 20 min, no discernable changes in the shape or pore structure of the core-shell nanoparticles were observed, indicating the stability and applicability as drug carriers for controlled release (Figure S3B). The photothermal efficiency was calculated and found to be 56.8% (See discussion in Supporting Information).

Next, we investigated the loading and controlled release of cargo from core-shell nanostructures using 1-tetradecanol as gate keeper. 1-Tetradecanol, a biocompatible phase changing material, exhibits melting temperature of 38–39°C, which is slightly above the normal human body temperature. Consequently, 1-tetradecanol can contain the cargo in the nanoparticles at body temperature with minimal leakage and enable triggered release of the contents by external heating.[50] A model dye, Rose Bengal (RB), mixed with 1-tetradecanol was loaded into the nanostructures. As discussed above, under NIR irradiation, PDA@$mSiO_2$ nanoparticles exhibited temperature rise, enough to melt 1-tetradecanol and release the cargo. The RB-loaded PDA@$mSiO_2$ was concentrated to 4 mg/ml and subjected

to NIR laser (14 mW/mm^2) to trigger the release. During the first 5 minutes of the treatment, the solution temperature raised steadily followed by saturation at ~70°C for the subsequent 15 min of irradiation (Figure 3C). As the temperature increased to above the melting point of the 1-tetradecanol within 1 minute, the optical absorbance of RB in the surrounding aqueous medium started to increase, indicating the NIR-triggered release of the dye from the nanoparticles (Figure 3C, D). The cumulative absorbance of the dye steadily increased for the subsequent 20 min indicating the continuous release of the dye from the nanostructures. In stark contrast, the RB-loaded PDA@mSiO_2 nanoparticles solution incubated at room temperature (25°C) for 1 day exhibited a leakage of only 1.5%, which shows their excellent ability to contain and release the payload only under an external trigger. Successful loading and controlled release of the payload from PDA@mSiO_2 nanoparticles was further confirmed using a fluorescent dye (see Figure S5A and discussion in Supporting Information).

Photothermal therapeutic efficacy and immune-stimulatory effect of gardi-mPDA nanoparticles:

Now we evaluated the *in vitro* photothermal therapeutic efficacy of the gardiquimod-loaded PDA@mSiO_2 (called gardi-mPDA henceforth) nanoparticles. The encapsulation efficiency of gardiquimod in nanoparticles was determined to be 11 ± 3 μg/mg (see Experimental section). B16-F10 melanoma cells were incubated with different concentrations of gardi-mPDA nanoparticles, followed by 10 minutes of laser irradiation (14 mW/mm^2). For all concentrations of gardi-mPDA nanoparticles, a significant decrease in viability was observed in NIR treated cells compared to cells without NIR treatment (Figure 3E). Importantly, without NIR irradiation, no toxicity was observed, indicating that the adjuvant-loaded particles by themselves are not cytotoxic. For efficient photothermal cytotoxicity the nanoparticles should physically interact with cancer cells. The nanoparticle-cell interaction was assessed by incubating B16-F10 cells with LT680-loaded PDA@mSiO_2 (LT680-mPDA) followed by confocal fluorescence microscopy. We observed punctate-like LT680 signal from the cells confirming physical nanoparticle-cell interaction (Figure S5B).

After confirming the *in vitro* photothermal therapeutic efficacy of the gardi-mPDA nanoparticles, we investigated their immuno-stimulatory potential upon NIR-triggered release of gardiquimod. Bone marrow derived dendritic cells (BMDCs) were treated with supernatants collected from gardi-mPDA (100 μg/ml) subjected to 10 minutes of NIR treatment. Concentration of secreted interleukin 6 (IL-6) and tumor necrosis factor-α (TNFα), which indicate the activation of BMDCs, were measured and compared to secretion levels of BMDCs treated with free gardiquimod. There was a significant increase in cytokine secretion following the treatment of BMDCs with supernatant of NIR treated gardi-mPDA nanoparticles compared to supernatant without NIR treatment (Figure 3F, G). Similar results were observed for upregulation of maturation markers (CD40 and CD80), where supernatants collected from NIR-treated nanoparticles led to significant increase in BMDC maturation as compared to without NIR treatment (Figure S4). It is important to note that CD40 and CD80 serve as co-stimulatory signal for efficient activation of $CD8^+$ T cells. These results indicate that gardiquimod can be released with external trigger and the photothermally released gardiquimod is therapeutically active.

Combined photothermal-immunotherapy effect of gardi-mPDA nanoparticles:

After confirming the *in vitro* photothermal therapeutic efficacy of PDA@$mSiO_2$ nanoparticles and immuno-stimulatory effect of gardi-mPDA nanoparticles independently, we set out to answer two key questions: (i) Does the NIR treatment of cancer cells incubated with gardi-mPDA nanoparticles release both the TAAs and adjuvant concurrently?; and (ii) is the released adjuvant from the cancer cells capable of causing immunostimulatory effect? To address these questions, B16-F10 cells were treated with LT680-mPDA and then loaded with a cell-permeable protein-labelling dye, carboxyfluorescein succinimidyl ester (CFSE). Here, LT680 serves as model drug loaded in mPDA and CFSE labelled intracellular proteins serve as representative tumor antigen. There was no spectral overalp in the absorption and emission spectra of LT680 and CFSE (Figure S5C). The cells were harvested and divided into two groups: with and without NIR treatment (Figure 4A). The supernatants collected from both groups were analyzed for LT680 and CFSE fluorescence. The NIR treatment demonstrated significant increase in fluorescence intensity of both LT680 and CFSE as compared to without NIR treatment (Figure 4B, C). These results indicate the ability of PDA@$mSiO_2$ nanoparticles to simultaneously release the loaded drug and protein antigen from the cells when treated with NIR light. Next, we incubated B16-F10 cells with gardi-mPDA nanoparticles and subjected them to NIR treatment to induce the release of gardiquimod from internalized and cell surface bound nanoparticles. Subsequently, BMDCs were treated with the above mentioned B16-F10 cell culture supernatant to assess the activation ability of the released gardiquimod. Clearly, the cell culture supernatant resulted in activation of BMDCs as evidenced by the increase in the secreted IL-6 concentration, further confirming the NIR-assisted release of gardiquimod from within the cancer cells and its immunomodulatory effects (Figure 4D).

In vivo photothermal efficiency and externally triggered release of payload:

To further investigate the photothermal efficacy of the PDA@$mSiO_2$ nanoparticles *in vivo*, subcutaneously inoculated B16-F10 mouse melanoma model was used. One day after the administration of the nanoparticles, tumors were irradiated with an NIR laser for 5 minutes (laser power 6 and 14 mW/mm^2). Mice without nanoparticle injection were employed as control group. After laser irradiation at a power density of 14 mW/mm^2 for 5 minutes, the tumor temperature for the control group without nanoparticle injection reached 40°C. In contrast, under identical irradiation conditions, the tumor temperature for the mouse injected with PDA@$mSiO_2$ nanoparticles, increased to 81 °C, indicating the high photothermal efficiency of PDA@$mSiO_2$ nanoparticles in converting NIR light to heat and inducing locoregional cell ablation (Figure S6A, B). *In vivo* fluorescence imaging of the tumors after injection of LT680-mPDA revealed nearly two-fold increase in fluorescence after subjecting the tumors to NIR irradiation for 5 minutes as compared to without NIR treatment, confirming that the dye encapsulated in nanoparticles, is diffusing outward and restoring fluorescence after successful NIR triggered release from the nanoparticles (Figure S6C, D).

In vivo therapeutic efficacy of gardi-mPDA:

After confirming *in vitro* photothermal therapeutic efficacy and successful release of payload under NIR irradiation, we investigated the therapeutic potential of gardi-mPDA *in*

vivo. The release of tumor antigen after photothermal ablation of tumor cells and concurrent release of adjuvant is critical for robust anti-tumor immune response. We employed B16-F10 melanoma model and intra-tumorally injected the gardi-mPDA nanoparticles followed by NIR treatment (808 nm, 14 mW/mm^2) (Figure 5A). The first step was to assess the biocompatibility of nanoparticles for which the body weight of the mice was monitored. No significant difference was observed in the body weight of the mice treated with PDA@$mSiO_2$ or gardi-mPDA nanoparticles indicating that the nanoparticles did not cause any severe systemic toxicity (Figure 5B). Tumor growth was monitored for different treatment groups and we noted that the gardi-mPDA nanoparticles treated with NIR resulted in significant inhibition of tumor growth compared to gardi-mPDA nanoparticles without NIR, PDA@$mSiO_2$ nanoparticles with NIR and PBS group (Figure 5C). The survival rate of mice treated with gardi-mPDA nanoparticles and NIR was ~57% at day 43, while all the other groups had 0% survival rate at day 30 (Figure 5D). Notably, the tumors for mice treated with PDA@$mSiO_2$-NIR exhibited inhibition in tumor growth (due to photothermal tumor ablation) until day 10–11 while the tumors for mice treated with PBS or gardi-mPDA without NIR demonstrated constant growth (Figure 5E, F, G). However, the effect of PDA@$mSiO_2$-NIR was not long-lasting as the tumor cells, which survived photothermal ablation started growing, ultimately resulting in the formation of tumors equivalent in size to that of gardi-mPDA group at day 19. Although PDA@$mSiO_2$-NIR group is expected to release abundant tumor associated antigens during photothermal ablation, the presence of antigen without adjuvant resulted in sub-optimal therapeutic effect. In the other control group where the mice were treated with gardi-mPDA, adjuvants were available to tumor resident antigen-presenting cells (APCs) as the nanoparticles are eventually expected to be uptaken by APCs followed by their activation (Figure 6).

In case of treatment group gardi-mPDA (without NIR) nanoparticles would be uptaken by tumor resident dendritic cells and the particles are expected to disintegrate in the endosomes, eventually releasing gardiquimod. The gardi-mPDA treated mice showed moderate inhibition in tumor growth, which is possibly due to the reversal of immuno-suppressive microenvironment in tumor caused by TLR7/8 agonism in DCs.[51] Moderate inhibition of tumor growth after treatment with gardiquimod has been observed previously.[42–43] More specifically gardiquimod is known to impart tumor-killing potential to plasmacytoid dendritic cells.[52] Although moderate inhibition of tumor growth was observed in mice treated with PDA@$mSiO_2$-NIR and gardi-mPDA without NIR, it was short-lived as it eventually lead to 100% mortality by day 30. Mice treated with gardi-mPDA-NIR demonstrated dramatic inhibition in tumor growth emphasizing the role of simultaneous release of antigen and adjuvant (Figure 5H). The released antigen and adjuvants from the photothermally ablated tumor cells are available to APCs, which are expected to migrate to the tumor draining lymph nodes where they activate the $CD8^+$ T cells. These effector immune T cells are capable of eradicating the residual tumors, which survive the primary photothermal ablation. The mice surviving primary tumor challenge were able to significantly inhibit growth of secondary tumors indicating the generation of long-term memory response, when compared to age-matched naïve mice (Figure 5I). The biocompatibility of these nanoparticles was further confirmed by histopathological staining.

We observed no signs of cell death, confirming no systemic toxicity in the visceral organs of the mice after treatment with gardi-mPDA-NIR (Figure 5J).

Since the primary tumors were temporarily attenuated by photothermal effect caused by PDA@mSiO$_2$-NIR, we reasoned if the increase in NIR treatment duration from 5 minutes to 10 minutes could result in complete ablation of tumor growth without the need for immunotherapy. We treated the mice with PDA@mSiO$_2$ and gardi-mPDA followed by NIR treatment for 10 minutes (Figure S9A). NIR treatment for 10 minutes was well tolerated by mice as it did not cause any decrease in the body weight of the mice (Figure S9B). Interestingly, both PDA@mSiO$_2$-NIR and gardi-mPDA-NIR resulted in significant inhibition of tumor growth (Figure S9C). While less than half (40%) of the mice in PDA@mSiO$_2$-NIR group survived at, 80% of mice in gardi-mPDA-NIR survived until day 46 with no observable signs of primary tumor (Figure S9D). In order to evaluate the long-term efficacy of both photothermal therapy and photothermal-immunotherapy the tumor-free mice from primary challenge were subjected to secondary tumor challenge on the opposite flank. It was observed that the mice treated with concurrent photothermal-immunotherapy had better resistance to tumor growth as compared to just photothermal therapy (Figure S9E). Taken together, these results emphasize the significance of both specificity associated with the tumor-associated antigens and immune-stimulatory capabilities of the adjuvant for generation of robust and long-lasting anti-tumor immune response.

In vivo immune status in tumor draining lymph node:

Systematic lymph node mapping of mouse has shown that inguinal lymph nodes receive afferent lymphatics from tumors inoculated in the flanks.[53–58] Therefore, we assessed the immune cell population in the tumor draining inguinal lymph nodes of the mouse. The population and activation status of immune cells in the tumor draining lymph nodes was assessed to understand the role of immune cells in therapeutic effect. Increased percentage of both T cells and dendritic cells (DCs) was observed in tumor draining lymph nodes of mice treated with gardi-mPDA-NIR. Specifically, presence of $CD3^+CD8^+$ T cells was analyzed, and we observed that while PDA@mSiO$_2$-NIR resulted in a modest increase in T cells, gardi-mPDA nanoparticles irrespective of the presence or absence of NIR resulted in almost two-fold increase in T cell count compared to PBS (Figure 6A). Maturation of DCs was assessed by measuring the expression levels of maturation markers (CD40, CD80, MHC II). We observed higher activation of DCs with gardi-mPDA treated groups compared to PDA@mSiO$_2$-NIR or PBS group. PDA@mSiO$_2$-NIR has relatively mild immuno-stimulatory potential in the absence of potent adjuvants. Despite having significant immuno-stimulatory effect, the influence of gardi-mPDA is non-specific because of lack of specific tumor associated antigen (Figure 6B, S7, S8). This signifies that the presence of both antigen and adjuvant is critical for generation of long-lasting immune response. Externally triggered NIR facilitated the release of both antigen and adjuvant simultaneously, thus orchestrating a highly potent tumor-specific immune response.

Conclusion

To summarize, we designed and synthesized a core-shell nanostructure based on highly biocompatible and completely biodegradable components, where the photothermal property of the core was integrated with NIR-responsive drug release properties of the shell for ultimately generating a robust and long-lasting anti-tumor immune response. PDA nanoparticles were employed as a photothermal core and mesoporous silica shell was used as the carrier for a mixture of phase-change material (1-tetradecanol) and immune-stimulating agent (gardiquimod). These nanoparticles were effectively uptaken by cancer cells and led to concurrent release of both antigen and adjuvant from the cancer cells upon NIR irradiation. The external trigger NIR facilitated spatiotemporal control of the therapeutic events for ultimately mounting a potent anti-tumor immune response. The core-shell nanoparticle design is universal and is amenable for loading other types of immunomodulatory or chemotherapeutic drugs or their combinations for synergistic effects. The versatility and unique design of these multifunctional nanoparticles can be harnessed for improved photothermal-immunotherapeutic treatments acting as a powerful platform for cancer treatment.

Supplementary Material

Refer to Web version on PubMed Central for supplementary material.

Acknowledgements

Dr. A. Seth and H. G. Derami contributed equally to this work. We acknowledge support from National Institutes of Health (R21 CA236652 and R01 CA141521). The authors would like to thank Dr. Delaram Shakiba for helping with confocal fluorescence microscopy, Prof. Jai Rudra for providing access to flow cytometer, and the Nano Research Facility (NRF) and Institute of Materials Science and Engineering (IMSE) at Washington University for providing access to electron microscopy facilities.

References

1. Vesely MD; Kershaw MH; Schreiber RD; Smyth MJ, Natural Innate and Adaptive Immunity to Cancer. Annu. Rev. Immunol 2011, 29 (1), 235–271. [PubMed: 21219185]
2. Dunn GP; Bruce AT; Ikeda H; Old LJ; Schreiber RD, Cancer Immunoediting: From Immunosurveillance to Tumor Escape. Nat. Immunol 2002, 3 (11), 991–998. [PubMed: 12407406]
3. O'Donnell JS; Teng MWL; Smyth MJ, Cancer Immunoediting and Resistance to T Cell-Based Immunotherapy. Nat. Rev. Clin. Oncol 2018.
4. Beatty GL; Gladney WL, Immune Escape Mechanisms as a Guide for Cancer Immunotherapy. Clin. Cancer Res 2015, 21 (4), 687. [PubMed: 25501578]
5. Mellman I; Coukos G; Dranoff G, Cancer Immunotherapy Comes of Age. Nature 2011, 480 (7378), 480–489. [PubMed: 22193102]
6. Disis ML, Mechanism of Action of Immunotherapy. Semin. Oncol 2014, 41, S3–S13.
7. Huang L; Xu H; Peng G, Tlr-Mediated Metabolic Reprogramming in the Tumor Microenvironment: Potential Novel Strategies for Cancer Immunotherapy. Cell Mol. Immunol 2018, 15 (5), 428–437. [PubMed: 29553135]
8. Bocanegra Gondan AI; Ruiz-de-Angulo A; Zabaleta A; Gómez Blanco N; Cobaleda-Siles BM; García-Granda MJ; Padro D; Llop J; Arnaiz B; Gato M; Escors D; Mareque-Rivas JC, Effective Cancer Immunotherapy in Mice by Polyic-Imiquimod Complexes and Engineered Magnetic Nanoparticles. Biomaterials 2018, 170, 95–115. [PubMed: 29656235]

9. Xu C; Nam J; Hong H; Xu Y; Moon JJ, Positron Emission Tomography-Guided Photodynamic Therapy with Biodegradable Mesoporous Silica Nanoparticles for Personalized Cancer Immunotherapy. ACS Nano 2019, 13 (10), 12148–12161. [PubMed: 31556987]
10. Seth A; Heo MB; Lim YT, Poly (Γ-Glutamic Acid) Based Combination of Water-Insoluble Paclitaxel and Tlr7 Agonist for Chemo-Immunotherapy. Biomaterials 2014, 35 (27), 7992–8001. [PubMed: 24954733]
11. Phuengkham H; Ren L; Shin IW; Lim YT, Nanoengineered Immune Niches for Reprogramming the Immunosuppressive Tumor Microenvironment and Enhancing Cancer Immunotherapy. Adv. Mater 2019, 31 (34), 1803322.
12. Rodell CB; Arlauckas SP; Cuccarese MF; Garris CS; Li R; Ahmed MS; Kohler RH; Pittet MJ; Weissleder R, Tlr7/8-Agonist-Loaded Nanoparticles Promote the Polarization of Tumour-Associated Macrophages to Enhance Cancer Immunotherapy. Nat. Biomed. Eng 2018, 2 (8), 578–588. [PubMed: 31015631]
13. Liu X; Yan S; Luo Z; Li Z; Wang Y; Tao J; Gong C, Improving Cancer Immunotherapy Outcomes Using Biomaterials. Angew. Chem., Int. Ed
14. Domvri K; Petanidis S; Anestakis D; Porpodis K; Bai C; Zarogoulidis P; Freitag L; Hohenforst-Schmidt W; Katopodi T, Dual Photothermal Mdscs-Targeted Immunotherapy Inhibits Lung Immunosuppressive Metastasis by Enhancing T-Cell Recruitment. Nanoscale 2020, 12 (13), 7051–7062. [PubMed: 32186564]
15. Liu Y; Lu Y; Zhu X; Li C; Yan M; Pan J; Ma G, Tumor Microenvironment-Responsive Prodrug Nanoplatform Via Co-Self-Assembly of Photothermal Agent and Ido Inhibitor for Enhanced Tumor Penetration and Cancer Immunotherapy. Biomaterials 2020, 242, 119933. [PubMed: 32151859]
16. Zhou L; Chen L; Hu X; Lu Y; Liu W; Sun Y; Yao T; Dong C; Shi S, A Cu9s5 Nanoparticle-Based Cpg Delivery System for Synergistic Photothermal-, Photodynamic- and Immunotherapy. Commun. Biol 2020, 3 (1), 343. [PubMed: 32620811]
17. Im S; Lee J; Park D; Park A; Kim Y-M; Kim WJ, Hypoxia-Triggered Transforming Immunomodulator for Cancer Immunotherapy Via Photodynamically Enhanced Antigen Presentation of Dendritic Cell. ACS Nano 2019, 13 (1), 476–488. [PubMed: 30563320]
18. Chen Q; Xu L; Liang C; Wang C; Peng R; Liu Z, Photothermal Therapy with Immune-Adjuvant Nanoparticles Together with Checkpoint Blockade for Effective Cancer Immunotherapy. Nat. Commun 2016, 7 (1), 13193. [PubMed: 27767031]
19. Yang W; Zhu G; Wang S; Yu G; Yang Z; Lin L; Zhou Z; Liu Y; Dai Y; Zhang F; Shen Z; Liu Y; He Z; Lau J; Niu G; Kiesewetter DO; Hu S; Chen X, In Situ Dendritic Cell Vaccine for Effective Cancer Immunotherapy. ACS Nano 2019, 13 (3), 3083–3094. [PubMed: 30835435]
20. Ye X; Liang X; Chen Q; Miao Q; Chen X; Zhang X; Mei L, Surgical Tumor-Derived Personalized Photothermal Vaccine Formulation for Cancer Immunotherapy. ACS Nano 2019, 13 (3), 2956–2968. [PubMed: 30789699]
21. Ni K; Luo T; Lan G; Culbert A; Song Y; Wu T; Jiang X; Lin W, Nanoscale Metal-Organic Frameworks Mediate Photodynamic Therapy and Deliver Cpg Oligodeoxynucleotides to Enhance Antigen Presentation and Cancer Immunotherapy. Angew. Chem., Int. Ed 2019, 0 (ja).
22. Embgenbroich M; Burgdorf S, Current Concepts of Antigen Cross-Presentation. Front. Immunol 2018, 9, 1643–1643. [PubMed: 30061897]
23. Sánchez-Paulete AR; Teijeira A; Cueto FJ; Garasa S; Pérez-Gracia JL; Sánchez-Arráez A; Sancho D; Melero I, Antigen Cross-Presentation and T-Cell Cross-Priming in Cancer Immunology and Immunotherapy. Ann. Oncol 2017, 28 (suppl_12), xii44–xii55. [PubMed: 28945841]
24. Alloatti A; Kotsias F; Magalhaes JG; Amigorena S, Dendritic Cell Maturation and Cross-Presentation: Timing Matters! Immunol. Rev 2016, 272 (1), 97–108. [PubMed: 27319345]
25. Gil-Torregrosa BC; Lennon-Duménil AM; Kessler B; Guermonprez P; Ploegh HL; Fruci D; Endert PV; Amigorena S, Control of Cross-Presentation During Dendritic Cell Maturation. Eur. J. Immunol 2004, 34 (2), 398–407. [PubMed: 14768044]
26. Reis e Sousa C, Dendritic Cells in a Mature Age. Nat. Rev. Immunol 2006, 6 (6), 476–483. [PubMed: 16691244]

27. Dhodapkar MV; Dhodapkar KM; Palucka AK, Interactions of Tumor Cells with Dendritic Cells: Balancing Immunity and Tolerance. Cell Death Differ 2008, 15 (1), 39–50. [PubMed: 17948027]
28. Makkouk A; Weiner GJ, Cancer Immunotherapy and Breaking Immune Tolerance: New Approaches to an Old Challenge. Cancer Res 2015, 75 (1), 5. [PubMed: 25524899]
29. Mende I; Engleman EG, Breaking Self-Tolerance to Tumor-Associated Antigens by in Vivo Manipulation of Dendritic Cells. In Immunological Tolerance: Methods and Protocols, Fairchild PJ, Ed. Humana Press: Totowa, NJ, 2007; pp 457–468.
30. Lee H; Dellatore SM; Miller WM; Messersmith PB, Mussel-Inspired Surface Chemistry for Multifunctional Coatings. Science (New York, N.Y.) 2007, 318 (5849), 426–430.
31. Liu X; Cao J; Li H; Li J; Jin Q; Ren K; Ji J, Mussel-Inspired Polydopamine: A Biocompatible and Ultrastable Coating for Nanoparticles in Vivo. ACS Nano 2013, 7 (10), 9384–9395. [PubMed: 24010584]
32. Zhang P; Xu Q; Du J; Wang Y, Polydopamine-Based Nanoparticles with Excellent Biocompatibility for Photothermally Enhanced Gene Delivery. RSC Adv 2018, 8 (60), 34596–34602.
33. Poinard B; Lam SAE; Neoh KG; Kah JCY, Mucopenetration and Biocompatibility of Polydopamine Surfaces for Delivery in an Ex Vivo Porcine Bladder. J. Controlled Release. 2019, 300, 161–173.
34. Gu GE; Park CS; Cho H-J; Ha TH; Bae J; Kwon OS; Lee J-S; Lee C-S, Fluorescent Polydopamine Nanoparticles as a Probe for Zebrafish Sensory Hair Cells Targeted in Vivo Imaging. Sci. Rep 2018, 8 (1), 4393. [PubMed: 29535354]
35. Ball V, Polydopamine Nanomaterials: Recent Advances in Synthesis Methods and Applications. Front. Bioeng. Biotechnol 2018, 6 (109).
36. Liu Y; Ai K; Lu L, Polydopamine and Its Derivative Materials: Synthesis and Promising Applications in Energy, Environmental, and Biomedical Fields. Chem. Rev 2014, 114 (9), 5057–5115. [PubMed: 24517847]
37. Yan S; Zeng X; Tang Y. a.; Liu B-F; Wang Y; Liu X, Activating Antitumor Immunity and Antimetastatic Effect through Polydopamine-Encapsulated Core–Shell Upconversion Nanoparticles. Adv. Mater 2019, 31 (46), 1905825.
38. Zhang P; Xu Q; Li X; Wang Y, Ph-Responsive Polydopamine Nanoparticles for Photothermally Promoted Gene Delivery. Mater. Sci.Engin.: C 2020, 108, 110396.
39. Poinard B; Neo SZY; Yeo ELL; Heng HPS; Neoh KG; Kah JCY, Polydopamine Nanoparticles Enhance Drug Release for Combined Photodynamic and Photothermal Therapy. ACS Appl. Mater. Int 2018, 10 (25), 21125–21136.
40. Chen R; Zhu C; Fan Y; Feng W; Wang J; Shang E; Zhou Q; Chen Z, Polydopamine-Based Multifunctional Platform for Combined Photothermal Therapy, Chemotherapy, and Immunotherapy in Malignant Tumor Treatment. ACS Appl. Bio. Mater 2019, 2 (2), 874–883.
41. Li W; Liu Z; Fontana F; Ding Y; Liu D; Hirvonen JT; Santos HA, Tailoring Porous Silicon for Biomedical Applications: From Drug Delivery to Cancer Immunotherapy. Adv. Mater 2018, 30 (24), 1703740.
42. Ma F; Zhang J; Zhang J; Zhang C, The Tlr7 Agonists Imiquimod and Gardiquimod Improve Dc-Based Immunotherapy for Melanoma in Mice. Cell Mol. Immunol 2010, 7 (5), 381–388. [PubMed: 20543857]
43. Seth A; Lee H; Cho MY; Park C; Korm S; Lee J-Y; Choi I; Lim YT; Hong KS, Combining Vasculature Disrupting Agent and Toll-Like Receptor 7/8 Agonist for Cancer Therapy. Oncotarget 2017, 8 (3), 5371–5381. [PubMed: 28036266]
44. Weber A; Zimmermann C; Mausberg AK; Kieseier BC; Hartung HP; Hofstetter HH, Induction of Pro-Inflammatory Cytokine Production in Thymocytes by the Immune Response Modifiers Imiquimod and Gardiquimod™. Int. Immunopharmacol 2013, 17 (2), 427–431. [PubMed: 23867290]
45. Zou BB; Wang F; Li L; Cheng FW; Jin R; Luo X; Zhu LX; Geng X; Zhang SQ, Activation of Toll-Like Receptor 7 Inhibits the Proliferation and Migration, and Induces the Apoptosis of Pancreatic Cancer Cells. Mol. Med. Rep 2015, 12 (4), 6079–6085. [PubMed: 26238718]

46. Ai K; Liu Y; Ruan C; Lu L; Lu G, Sp2 C-Dominant N-Doped Carbon Sub-Micrometer Spheres with a Tunable Size: A Versatile Platform for Highly Efficient Oxygen-Reduction Catalysts. Adv. Mater 2013, 25 (7), 998–1003. [PubMed: 23239109]
47. Moon GD; Choi S-W; Cai X; Li W; Cho EC; Jeong U; Wang LV; Xia Y, A New Theranostic System Based on Gold Nanocages and Phase-Change Materials with Unique Features for Photoacoustic Imaging and Controlled Release. J. Amer. Chem. Soc 2011, 133 (13), 4762–4765. [PubMed: 21401092]
48. Wang C; Ma Z; Wang T; Su Z, Synthesis, Assembly, and Biofunctionalization of Silica-Coated Gold Nanorods for Colorimetric Biosensing. Adv. Funct. Mater 2006, 16 (13), 1673–1678.
49. Shen S; Tang H; Zhang X; Ren J; Pang Z; Wang D; Gao H; Qian Y; Jiang X; Yang W, Targeting Mesoporous Silica-Encapsulated Gold Nanorods for Chemo-Photothermal Therapy with near-Infrared Radiation. Biomaterials 2013, 34 (12), 3150–3158. [PubMed: 23369218]
50. Tian L; Gandra N; Singamaneni S, Monitoring Controlled Release of Payload from Gold Nanocages Using Surface Enhanced Raman Scattering. ACS nano 2013, 7 (5), 4252–4260. [PubMed: 23577650]
51. Tran TH; Tran TTP; Truong DH; Nguyen HT; Pham TT; Yong CS; Kim JO, Toll-Like Receptor-Targeted Particles: A Paradigm to Manipulate the Tumor Microenvironment for Cancer Immunotherapy. Acta Biomater 2019, 94, 82–96. [PubMed: 31129358]
52. Stary G; Bangert C; Tauber M; Strohal R; Kopp T; Stingl G, Tumoricidal Activity of Tlr7/8-Activated Inflammatory Dendritic Cells. J. Exp. Med 2007, 204 (6), 1441–1451. [PubMed: 17535975]
53. Chin CS; Bear HD, Sentinel Node Mapping Identifies Vaccine-Draining Lymph Nodes with Tumor-Specific Immunological Activity. Ann. Surg. Oncol 2002, 9 (1), 94–103. [PubMed: 11829435]
54. Harrell MI; Iritani BM; Ruddell A, Lymph Node Mapping in the Mouse. J. Immunol. Methods 2008, 332 (1), 170–174. [PubMed: 18164026]
55. Yokoyama H; Nakanishi H; Kodera Y; Ikehara Y; Ohashi N; Ito Y; Koike M; Fujiwara M; Tatematsu M; Nakao A, Biological Significance of Isolated Tumor Cells and Micrometastasis in Lymph Nodes Evaluated Using a Green Fluorescent Protein–Tagged Human Gastric Cancer Cell Line. Clin. Cancer Res 2006, 12 (2), 361. [PubMed: 16428473]
56. Woglom WH, Metastasis to the Lymph Nodes from Mouse Sarcoma 37. Amer. J. Cancer 1940, 38 (3), 328.
57. Proulx ST; Luciani P; Christiansen A; Karaman S; Blum KS; Rinderknecht M; Leroux J-C; Detmar M, Use of a Peg-Conjugated Bright near-Infrared Dye for Functional Imaging of Rerouting of Tumor Lymphatic Drainage after Sentinel Lymph Node Metastasis. Biomaterials 2013, 34 (21), 5128–5137. [PubMed: 23566803]
58. Chandrasekaran S; Chan MF; Li J; King MR, Super Natural Killer Cells That Target Metastases in the Tumor Draining Lymph Nodes. Biomaterials 2016, 77, 66–76. [PubMed: 26584347]

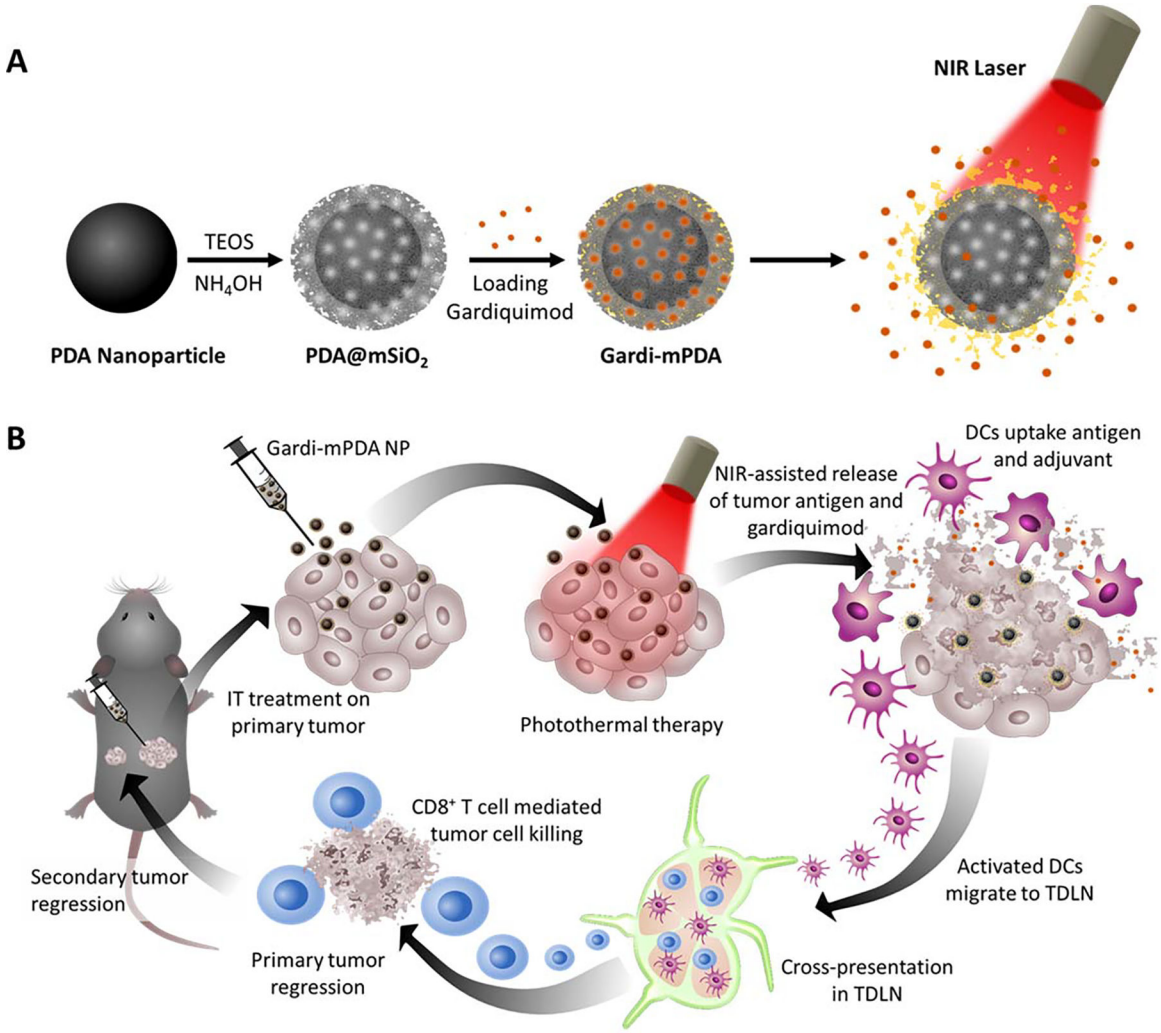

Figure 1.

Schematic illustrations depicting (A) Synthesis of gardiquimod-loaded mesoporous silica coated polydopamine nanoparticles (gardi-mPDA) and NIR-assisted drug release. (B) Tumor ablation and drug release under NIR irradiation followed by activation of DCs and effector T cells in tumor draining lymph nodes for regression of primary and secondary tumors.

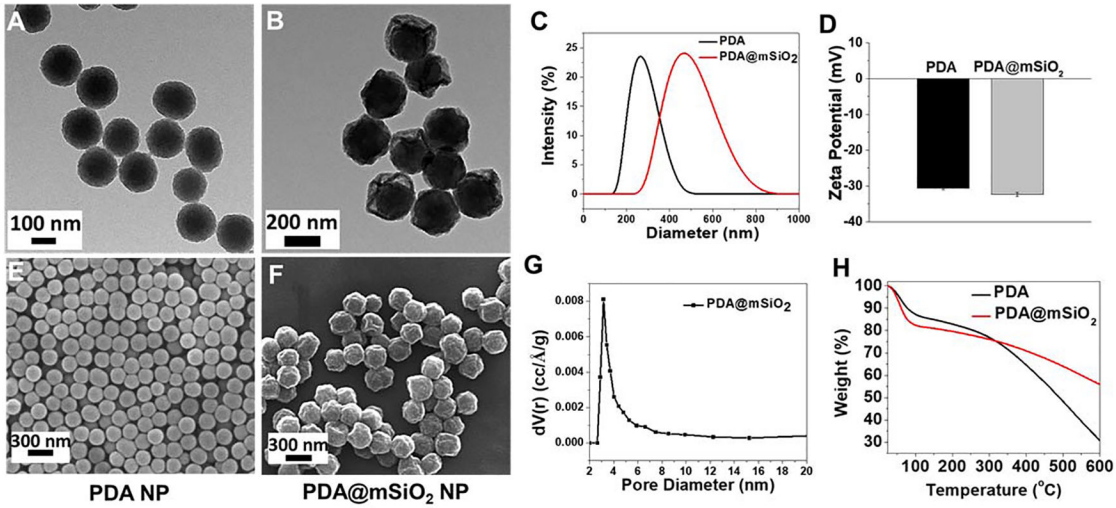

Figure 2.

TEM images of the (A) PDA and (B) PDA@$mSiO_2$ nanoparticles. (C) hydrodynamic diameter and (D) zeta potential of the PDA and PDA@$mSiO_2$ nanoparticles. SEM images of the (E) PDA and (F) PDA@$mSiO_2$ nanoparticles. (G) Pore size distribution of PDA@$mSiO_2$ nanoparticles obtained by nitrogen adsorption and using Barrett-Joyner-Halenda (BJH) method. (H) Weight loss profiles of PDA and PDA@$mSiO_2$ nanoparticles as measured by thermogravimetric analysis.

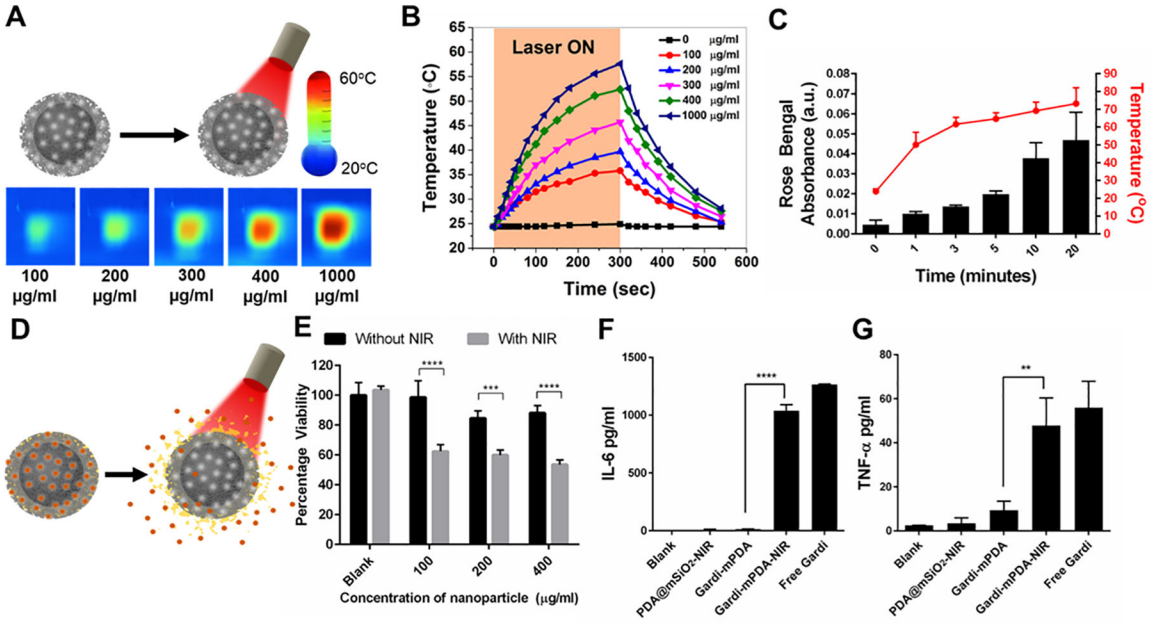

Figure 3.

(A) Schematic representation of NIR irradiation of pristine PDA@mSiO$_2$ nanoparticles and IR images of temperature rise with increase in particle concentration after 5 minutes of NIR laser treatment. (B) Temperature profile and effect of PDA@mSiO$_2$ particle concentration on temperature rise when aqueous solutions were subjected to laser power density of 14 mW/mm^2. (C) Cumulative release of model dye from the PDA@mSiO$_2$ nanoparticles after different laser irradiation durations and their corresponding solution temperature (laser power density, 14 mW/mm^2). (D) Schematic representation of gardiquimod loaded PDA@mSiO$_2$ (gardi-mPDA) nanoparticles and release of cargo with NIR treatment. (E) Cancer cell viability after treatment with gardi-mPDA with and without NIR. BMDC activation indicated by cytokine secretion (F) IL-6 and (G) TNFα. Data represented as mean ± SD. ** p<0.01, *** p<0.001 and **** p<0.0001 by one-way ANOVA with Tukey's posttest.

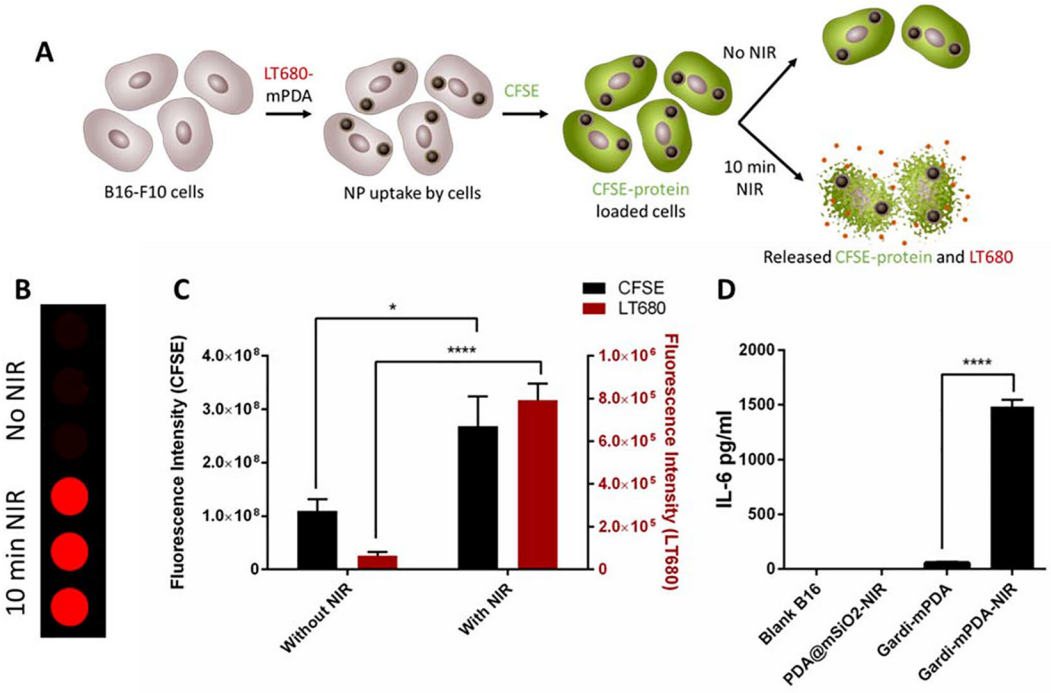

Figure 4.

Combined photothermal-immunotherapy effect in the presence of NIR. (A) Schematic illustration describing the experiment. Briefly, B16-F10 cells were treated with LT680-mPDA followed by labelling with CFSE. The labelled cells were divided into 2 groups and one group was given NIR treatment for 10 min. The supernatant of 2 groups were collected after 12 hours and fluorescence intensity was measured. (B) Fluorescence images (LT680) of supernatants collected from cells treatment with and without NIR, (C) Fluorescence intensity of CFSE and LT680 with and without NIR, (D) IL-6 secretion by BMDCs treated with supernatants released from B16-F10 cells. Data represented as mean ± SD. * $p<0.05$ and **** $p<0.0001$ by one-way ANOVA with Tukey's posttest.

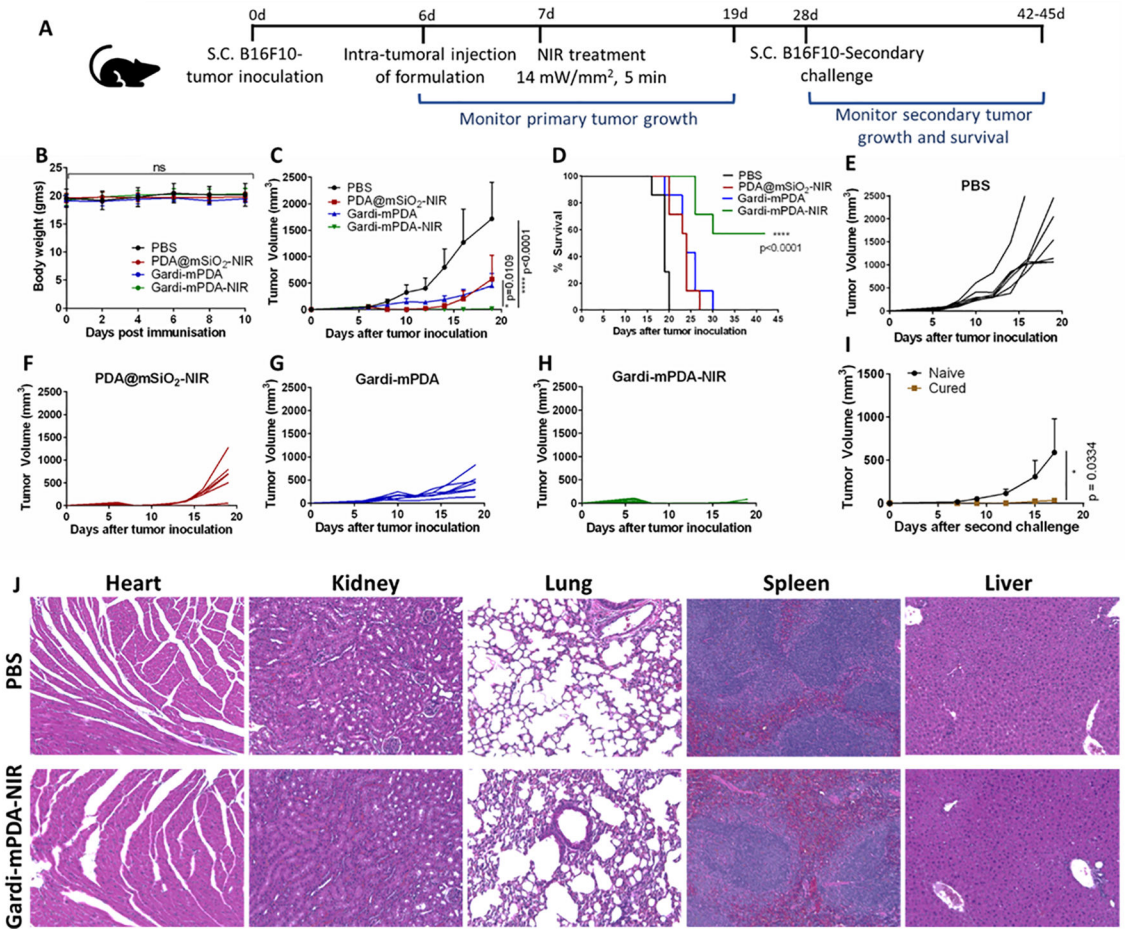

Figure 5.

In vivo photothermal-immunotherapeutic effect of gardi-mPDA.(A) Timeline of experiment. (B) *In vivo* toxicity of gardi-mPDA and NIR assessed by change in body weight of the mice, (C) tumor growth profiles, (D) survival curve of mice given different treatments (n=7). Tumor growth curves of individual mouse after treatment with (E) PBS, (F) PDA@$mSiO_2$-NIR, (G) gardi-mPDA and (H) gardi-mPDA-NIR. (I) Tumor volume after secondary challenge in mice surviving after gardi-mPDA-NIR treatment (cured mice) and age matched naïve mice (n=3). (J) Hematoxylin−eosin (H&E) staining images of major mice organs after treatment with PBS and gardi-mPDA-NIR. Data represented as mean ± SD. * $p<0.05$ and **** $p<0.0001$ by one-way ANOVA with Tukey's posttest and Log-rank (Mantel-Cox) test for survival curve.

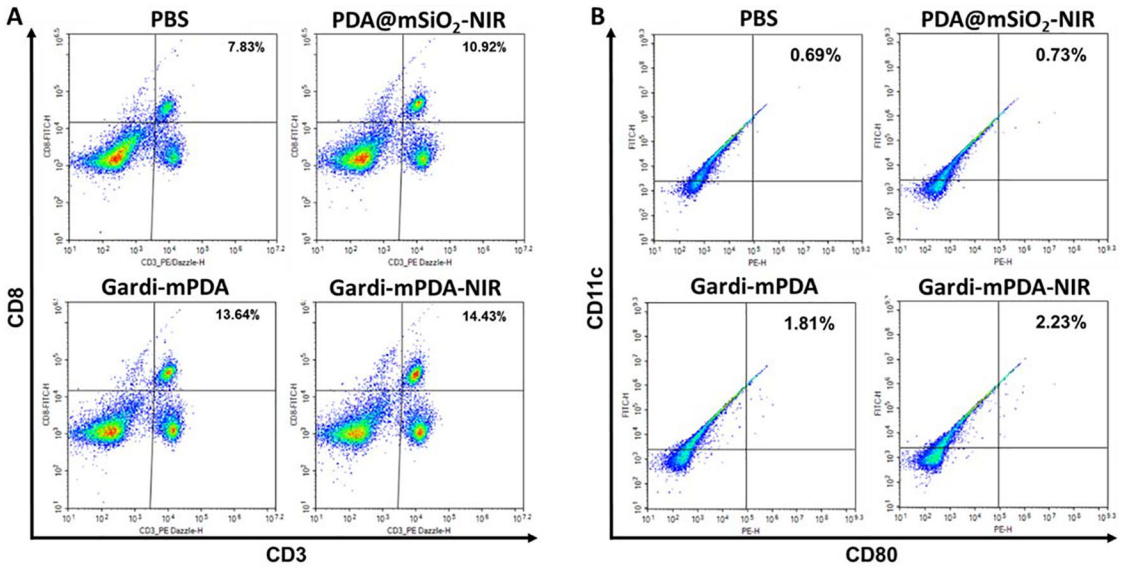

Figure 6.

Relative populations and activation status of immune cells in tumor draining lymph node at day 16. Representative flow cytometry plots of (A) $CD3^+$ $CD8^+$ T cells, (B) $CD11c^+$ $CD80^+$ dendritic cells. Percentage positive cells are displayed on top right corner.